Particle-hole symmetry broken solutions in graphene nanoribbons: A multi-orbital, mean-field perspective

T. Schmirander,* D. Pfannkuche, and M. Prada†
I. Institute for Theoretical Physics, Universität Hamburg, D-22761 Hamburg, Germany

(Received 2 November 2021; revised 23 June 2022; accepted 27 June 2022; published 7 July 2022)

Mean-field theories have since long predicted edge magnetism in graphene nanoribbons, where the order parameter is given by the local magnetization. However, signatures of edge magnetism appear elusive in the experiments, suggesting another class of solutions. We employ a self-consistent mean-field approximation within a multi-orbital tight-binding model and obtain particle-hole symmetry broken solutions, where the local filling plays the role of the order parameter. Unlike the magnetic edge solutions, these are topologically nontrivial and show zero local magnetization. A small and a large doping regime are studied, and a free energy minimum for finite hole doping is encountered, which may serve as an explanation for the absence of experimental evidence for magnetic edge states in zigzag graphene nanoribbons. The electronic interaction may increase the finite d-orbital occupation, which leads to a change of the effective Coulomb interaction of the dominant p_z orbitals. Our findings indicate that the nonmagnetic solution for finite hole doping becomes energetically preferred, compared to the magnetic phases at half filling, once thermal fluctuations or unintentional doping from the substrate are considered. This result persists even in the presence of the d orbitals and the Coulomb interaction therein.

DOI: 10.1103/PhysRevB.106.045407

I. INTRODUCTION

Graphene nanoribbons with zigzag edges belong to the class of topological matter with insulating bulk and conducting edges [1–3]. The Fermi level crossing states were predicted to give rise to a novel type of magnetic ordering [4], leading to appealing carbon-based magnetic materials and stimulating a large number of proposals of novel graphene-based spintronic devices [5–10]. Many experiments have ever since claimed to prove the existence of magnetism at the edges [11,12], but the accuracy of these findings allow for explanations other than the occurrence of magnetic edge states [13]. A gap opening in the local density of states has been found, which is consistent with magnetic ordering of the edge phases [14–16], but experiments usually probe only either the edge character of electronic states in graphene or the alignment of the spin degree of freedom. This poses the first problem of experimental verification of the topologically insulating phase of graphene that is still unresolved: Is the ground state of graphene nanoribbons truly nonmagnetic or has it just not been measured yet?

The description of noninteracting graphene is usually performed by employing the Kane-Mele model [17–19], which distinguishes between a trivial and a nontrivial phase in terms of external parameters. This is commonly extended to the interacting Kane-Mele-Hubbard model [20–23]. While such considerations apply to bulk graphene, coupling of the edge states in terminated structures leads to an energy gap in the magnetic ground state [24–26], which can be described by an *interedge superexchange* [27,28]. This mechanism predicts a zero-spin ground state, where the magnetic edges show opposite polarization. Different types of interedge magnetism can occur in graphene nanoribbons at half filling [3,29], namely, the antiferromagnetic (AFM) and the ferromagnetic state (FM), but other states with different degrees of edge magnetism are also possible once doping is considered [5,30]. The particle-hole symmetry (PHS) is broken in a doped system, and a completely nonmagnetic phase is possible, as the Fermi energy is located away from the magnetic instability. This phase may play a central role in realistic structures, as unintentional doping or commonly used substrates (SiO_2 [31], SiC [32], or h-BN [33]) has been shown to shift the Fermi level off the half filling condition at the Dirac points (DPs), and hence, broken PHS is expected in the experiments. Edge states in graphene nanoribbons are commonly examined by using density-functional theory (DFT) of the π orbitals in graphene [34,35], where the mean-field method remains a good approximation for realistic interactions [36].

The atomic or intrinsic d-orbital spin-orbit coupling becomes relevant for the size of the gap at the Dirac points of graphene [37,38] and should not be neglected. Moreover, it provides helicity to the edge states [18,39,40]. This leads to the second problem of detecting edge magnetism in graphene, namely, the influence of the electronic interaction of the d-orbital electrons on the π orbitals in a realistic—or doped—system, which has not been examined to this date.

This paper is intended to address these two problems by defining a multi-orbital tight-binding model with p_z and d orbitals, and is organized as follows: In Sec. II we describe the multi-orbital tight-binding model and the

*tschmira@physnet.uni-hamburg.de
†mprada@physnet.uni-hamburg.de

TABLE I. Hopping matrix elements $t_{ij}^{\alpha\beta}$. (l, m) are the directive cosines connecting the neighboring sites i and j [37,41]. The corresponding tight-binding parameters are given in Table II.

α, β	p_z	d_{xz}	d_{xz}
p_z	$V^{pp\pi}$	$lV^{pd\pi}$	$mV^{pd\pi}$
d_{xz}	$-lV^{pd\pi}$	$l^2V^{dd\pi} + m^2V^{dd\delta}$	$lm(V^{dd\pi} - V^{dd\delta})$
d_{yz}	$-mV^{pd\pi}$	$lm(V^{dd\pi} - V^{dd\delta})$	$m^2V^{dd\pi} + l^2V^{dd\delta}$

self-consistent mean-field method. We present numerical results of the single-orbital and multi-orbital models in Sec. III, by comparing the two magnetic phases and by examining the nonmagnetic phase in detail. We summarize our results in Sec. IV.

II. METHODS

The basis of our multi-orbital tight-binding model is spanned by p_z-, d_{xz}-, and d_{yz} orbitals localized at the sites of the honeycomb lattice. The other three d orbitals couple only weakly to the π bands via d-orbital spin-orbit coupling (SOC) and thus can be neglected in the neighborhood of the Fermi level. Hopping among nearest-neighboring sites $\langle ij\rangle$ is enabled by a term

$$H_0 = \sum_{\langle i,j\rangle,\alpha,\beta,\sigma} t_{ij}^{\alpha\beta}\hat{c}_{i\alpha\sigma}^{\dagger}\hat{c}_{j\beta\sigma}, \tag{1}$$

where the indices $\alpha, \beta \in \{p_z, d_{xz}, d_{yz}\}$ label the different orbitals and $\hat{c}_{i\alpha\sigma}^{(\dagger)}$ are the annihilation (creation) operators for spin σ. The hopping matrix elements are given within the Slater-Koster approximation [41], which are defined in Table I. The corresponding parameters are presented in Table II. Owing to symmetry, the intrinsic SOC is only nonzero for the d orbitals that constitute the π band:

$$H_{\mathrm{SOC}}^{i} = \xi_d \sum_{\alpha,\beta,\sigma,\sigma'} \langle \vec{L}\cdot\vec{S}\rangle_{\alpha\beta}^{i}\hat{c}_{i\alpha\sigma}^{\dagger}\hat{c}_{i\beta\sigma'} \tag{2}$$

with $\xi_d = 0.8$ meV [37] and $\langle \vec{L}\cdot\vec{S}\rangle_{d_{\alpha z}d_{\beta z}}^{i} = i\epsilon_{\alpha\beta z}s_z$, with s_z being the z component of the spin. Note that, although the prefactor is very small compared with other energy scales of the system, SOC introduces broken spin-rotations and defines the quantization direction.

The on-site energy of the different orbitals is given by

$$H_E^{i} = \sum_{\alpha,\sigma} E_\alpha \hat{c}_{i\alpha\sigma}^{\dagger}\hat{c}_{i\alpha\sigma}, \tag{3}$$

where we choose for convenience $E_p = 0$, yielding $E_d = 12$ eV.

For the Coulomb interaction, it is convenient to express the density operators $\hat{n}_{i\alpha\sigma} = \langle\hat{n}_{i\alpha\sigma}\rangle + \Delta\hat{n}_{i\alpha\sigma}$, where $\langle\hat{n}_{i\alpha\sigma}\rangle$ is the mean value of the density and $\Delta\hat{n}_{i\alpha\sigma}$ its fluctuation. As it is customary in the mean-field approximation, quadratic-in-fluctuations terms are neglected, yielding for the interacting Hamiltonian for site i:

$$\begin{aligned} H_{\mathrm{ee}}^{i} = \sum_{\sigma}\frac{U}{2}(\langle\hat{n}_{ip\bar{\sigma}}\rangle\hat{n}_{ip\sigma} + \langle\hat{n}_{ip\sigma}\rangle\hat{n}_{ip\bar{\sigma}} - \langle\hat{n}_{ip\bar{\sigma}}\rangle\langle\hat{n}_{ip\sigma}\rangle) + \sum_{\lambda,\sigma}[V(\langle\hat{n}_{ip\sigma}\rangle\hat{n}_{i\lambda\bar{\sigma}} + \langle\hat{n}_{i\lambda\sigma}\rangle\hat{n}_{ip\bar{\sigma}} - \langle\hat{n}_{ip\bar{\sigma}}\rangle\langle\hat{n}_{i\lambda\sigma}\rangle) \\ + J(\langle\hat{c}_{i\lambda\bar{\sigma}}^{\dagger}\hat{c}_{ip\bar{\sigma}}\rangle\hat{c}_{ip\sigma}^{\dagger}\hat{c}_{i\lambda\sigma} + \langle\hat{c}_{ip\sigma}^{\dagger}\hat{c}_{i\lambda\sigma}\rangle\hat{c}_{i\lambda\bar{\sigma}}^{\dagger}\hat{c}_{ip\bar{\sigma}} - \langle\hat{c}_{ip\sigma}^{\dagger}\hat{c}_{i\lambda\sigma}\rangle\langle\hat{c}_{i\lambda\bar{\sigma}}^{\dagger}\hat{c}_{ip\bar{\sigma}}\rangle) + (V-J)(\langle\hat{n}_{ip\sigma}\rangle\hat{n}_{i\lambda\sigma} \\ + \langle\hat{n}_{i\lambda\sigma}\rangle\hat{n}_{ip\sigma} - \langle\hat{n}_{i\lambda\sigma}\rangle\langle\hat{n}_{ip\sigma}\rangle - \langle\hat{c}_{ip\sigma}^{\dagger}\hat{c}_{i\lambda\sigma}\rangle\hat{c}_{i\lambda\sigma}^{\dagger}\hat{c}_{ip\sigma} - \langle\hat{c}_{i\lambda\sigma}^{\dagger}\hat{c}_{ip\sigma}\rangle\hat{c}_{ip\sigma}^{\dagger}\hat{c}_{i\lambda\sigma} + \langle\hat{c}_{i\lambda\sigma}^{\dagger}\hat{c}_{ip\sigma}\rangle\langle\hat{c}_{ip\sigma}^{\dagger}\hat{c}_{i\lambda\sigma}\rangle)], \end{aligned} \tag{4}$$

where p labels a p_z orbital and $\lambda \in \{d_{xz}, d_{yz}\}$ labels a d orbital, with σ and $\bar{\sigma}$ indicating opposite spin. Here, U is the Hubbard term, that is, the on-site Coulomb repulsion for the p_z orbitals, whereas V denotes the Coulomb repulsion and exchange, respectively, between a p_z and a d orbital. U is on the order of $V^{pp\pi}$, which has been obtained by comparing single-orbital tight-binding models with DFT calculations [43,44]. As prognosed by Hubbard [45] and employed elsewhere [46], V is on the order of U, while J is around an order of magnitude smaller. V and J serve here as parameters to quantify their influence on the characteristics and internal energy of the different phases, as these cannot be obtained from experiments [5]. It is worth noting that the nonlocal Coulomb interactions in the zigzag nanoribbons considered here are strongly screened by the edge states [47] and hence, we restrict the interactions to the local Coulomb terms described in Eq. (4). We note that the broken spin rotations introduced by the Coulomb interaction of Eq (4) renders the SOC term irrelevant in most of our calculations, however, it avoids numerical ambiguities.

Combining all terms described above, the total Hamiltonian for this multi-orbital tight-binding model reads

$$H = H_0 + \sum_i \left(H_E^{i} + H_{\mathrm{SOC}}^{i} + H_{\mathrm{ee}}^{i}\right), \tag{5}$$

where the first term is off-diagonal, while the rest contain on-site terms only. It is thus advantageous to Fourier transform Eq. (5) and solve the eigenvalue problem self-consistently via direct diagonalization, where periodic boundary conditions are applied along the edges of the nanoribbon [see inset of

TABLE II. The tight-binding parameters for graphene as used in the Slater-Koster approximation [37,42].

$V^{pp\pi}$	$V^{pd\pi}$	$V^{dd\pi}$	$V^{dd\delta}$	$V^{pp\sigma}$	$V^{pd\sigma}$	$V^{dd\sigma}$	E_d	E_p
−3 eV	−0.69 eV	−0.3 eV	2.25 eV	−8.1 eV	3.6 eV	3 eV	12 eV	0 eV

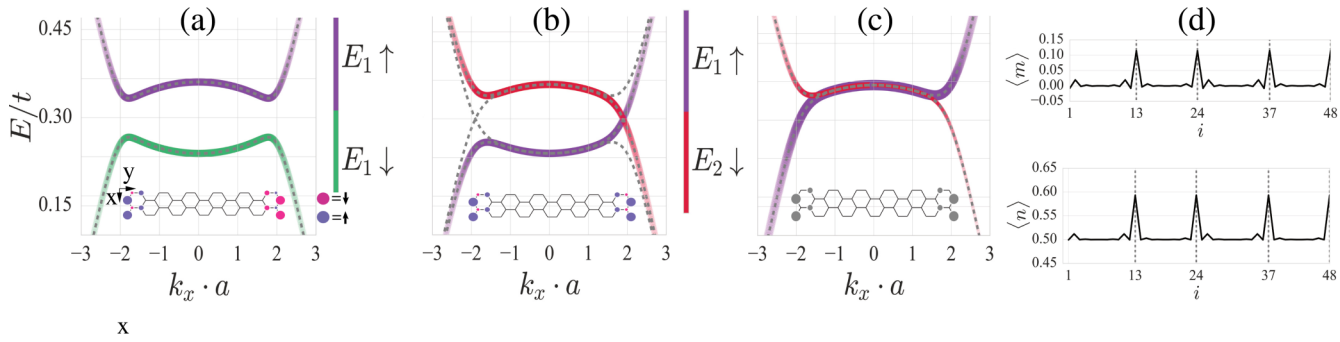

FIG. 1. Dispersion relation of a Kramers pair of the different solutions to the mean-field problem for a $N = 12$ ribbon computed for the single-orbital model. The bands are colored by edge (E_1/E_2) and real spin ($\uparrow$ / $\downarrow$). The Kramers pairs can be obtained by TR symmetry. (a) AFM phase. (b) FM phase. (c) The PHS broken nonmagnetic phase with $\delta n = 0.08$. Lower inset in [(a),(b)] depict the corresponding local magnetization or local additional occupation of (c). Note that periodic boundary conditions are applied along x (vertical direction in the insets). (d) Local magnetization $\langle m \rangle$ for the ground state of (a) and local density $\langle n \rangle$ corresponding to (c).

Fig. 1(a)]. The density of states is then numerically obtained by sampling 801 points across the Brillouin zone, where a Gaussian broadening is optimized after a convergence study. A temperature of $k_B T = 3.45 \times 10^{-4}$ eV is defined for convergence purposes, allowing the computation of the Fermi energy E_F [48].

III. NUMERICAL RESULTS

A. Three different phases

As it is habitual in self-consistent methods, the character of the converged solution reflects that of the initial guess. Breaking time-reversal (TR) symmetry by starting with parallel spin edges leads to a magnetic phase with a finite total spin-magnetic moment, whereas an initial state with polarized edges of opposite sign leads to a solution with broken spin rotations and zero total spin. In both cases, half filling is imposed. Another possibility (although commonly ignored), is to consider TR-symmetric solutions with broken electron-hole symmetry, namely, a doped solution. This can be achieved by an initial state with an excess of holes or electrons, and usually converges to a nonmagnetic phase. In what follows, we distinguish between magnetic and nonmagnetic solutions. The former occurs at half filling, $\langle n_i \rangle = 0.5$, whereas the latter has no local magnetization. The order parameter of this nonmagnetic, PHS broken solution is given in terms of the local doping δn_i, giving the local occupation per spin of $\langle n_i \rangle = 0.5 + \delta n_i$, whereas the magnetic phase is characterized by a finite local magnetization $\langle m_i \rangle$.

We consider first a single-orbital (p_z) model in a nanoribbon with $N = 12$ rows and 4 columns, using $U = 0.6t$. States with local ferrimagnetic spin polarization close to the edges have already been theoretically obtained [4,6,26,49–51], where the edges may exhibit parallel (FM) or antiparallel (AFM) spin alignment with respect to each other. Figure 1 contains the dispersion relation of the mid-bands, where bright color indicates edge-localized state. These bands are mainly located at the edges (E_1, E_2) of the sample, such that the components of these Kramers pairs are localized at the opposite edge [51]. The AFM solution in (a) corresponds to a trivial insulator, with a gap arising from the broken rotational symmetry [52]: From a symmetry perspective, the $E_2 \uparrow$ state is degenerate with the $E_1 \downarrow$ one and vice versa, but these states are not related by a rotation. From an interaction picture, the AFM exchange interaction acts as a staggered sublattice potential, which introduces a spin-dependent gap for states localized at different edges [18,53]. Figure 1(b) shows the FM solution, where two states with opposite spin cross the band gap. The coupling mechanism of states localized at two opposing edges can be described in analogy to the super exchange mechanism [27,54]. From a topological standpoint, chiral symmetry is the reason for the occurrence of gap-crossing states [2] of opposite Fermi velocity [55], whereas from a group symmetry perspective, these solutions maintain invariance with respect to the twofold axis, unlike the AFM case.

An additional phase is encountered in this paper, namely, a nonmagnetic PHS-broken solution, see Fig. 1(c), where the additional p_z-orbital occupation shifts the Fermi energy above $U/2$. The electronic occupation is symmetrically distributed along the edges of the sample, maintaining the original C_{2v} point group of the lattice. This results in a topologically nontrivial phase, just like in the noninteracting spin-Hall insulating case [17]. The corresponding order parameters are depicted in Fig. 1(d), that is, the on-site magnetization $\langle m_i \rangle = \frac{1}{2}(\langle \hat{n}_{i,\uparrow} \rangle - \langle \hat{n}_{i,\downarrow} \rangle)$ for the magnetic phases and the occupation for the PHS-broken solution, $\langle n_i \rangle = \frac{1}{2}(\langle \hat{n}_{i,\uparrow} \rangle + \langle \hat{n}_{i,\downarrow} \rangle)$. Values are plotted as a function of the site index i in sequence that follows columns (left to right) and rows (top to bottom) of the unit cell depicted in the insets of Figs. 1(a)–(c). For the FM solution, the magnetization is largest at the edge sites, with an exponential decay towards the bulk. The AFM phase (not shown) has similar magnetization, only with opposite sign at each edge. The PHS broken solution lacks of magnetic moments, however, the electronic occupation off half filling shows a similar behavior as $\langle m \rangle$ in the magnetic solutions. We stress that a similar solution with negative occupation off half filling (or hole-doped) is also found when the initial state has a filling slightly below half filling, where the occupation of the edge's sites is, respectively, $\langle n_E \rangle \sim 0.5 \pm 0.1$.

It is worth mentioning that the topologically trivial AFM solution minimizes the free energy when the half-filling condition is imposed. However, dopants change this criterion and

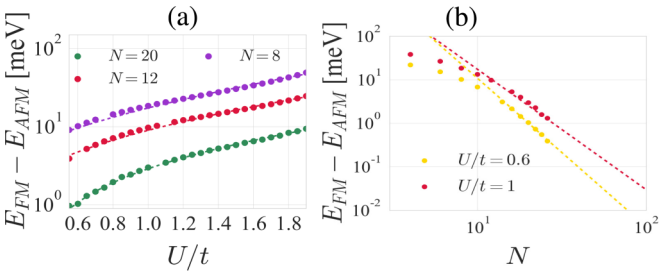

FIG. 2. Energy differences of FM and AFM phases for (a) $N = 8$, 12 and 20 as a function of U and (b) for $U/t = 0.6$ and $U/t = 1$, as a function of number of rows N. The dashed lines are polynomial fits (see text).

allows for a PHS broken state. In what follows we examine the free energy, the local magnetization, and the occupation of these three solutions as a function of ribbon size and interaction parameters in single and multi-orbital approach.

B. Energetic considerations

Lieb's theorem states that the ground state at half filling has zero spin-magnetic moment [56]. It follows that the ground state at half filling is always the AFM edge phase, regardless of ribbon size and for all $U > 0$. However, Lieb's theorem does not apply for doped systems, allowing for a ground state without any local spin-magnetic moment. We first compute and analyze the free energy of the three phases within the single-orbital model, and extend our computation to the multi-orbital model.

1. Single-orbital model

We first employ a single-orbital (p_z) model, where $t_{ij} = V^{pp\pi} \equiv t$ in Eq. (1), and with the Hubbard term being the only interacting term. We compute the free energy of the ground state for the different solutions. In Fig. 2(a) the energy differences of the two magnetic phases at half filling for three different ribbon sizes $N = 8$, 12, and 20 is shown as a function of U, where the AFM phase is found to always be lower in energy. As expected, the energy separation between both phases increases with the interaction parameter U. For $N = 8$, the reduced edge separation results in a relative lower energy of the AFM due to the interedge super exchange mechanism [27]. For larger N this energy gain becomes smaller and a law $\sim N^c$ with $c < -1$ is reproduced for moderate U. Figure 2(b) shows the behavior of the energy separation $E_{\mathrm{FM}} - E_{\mathrm{AFM}}$ as a function of the sample width N. The fittings (dashed lines) correspond to a power law aN^c for $N > 10$, to avoid finite size effects. The exponents $c = -3.41$ and $c = -2.74$ are extracted for $U = 0.6$ and 1, respectively. Note that finite-size effects within a mean-field model causes a deviation from the value reported by Jung *et al.* [27], $c = -2$. Hence, it is to be expected that in the thermodynamic limit $N \to \infty$ both magnetic phases become equally probable, as $|E_{\mathrm{FM}} - E_{\mathrm{AFM}}| \ll k_B T$.

We consider next the PHS broken solutions, where the Stoner criterion justifies the absence of magnetism in doped systems, as an increase of the Fermi energy above the peak in the density of states removes the magnetic instability [28,46].

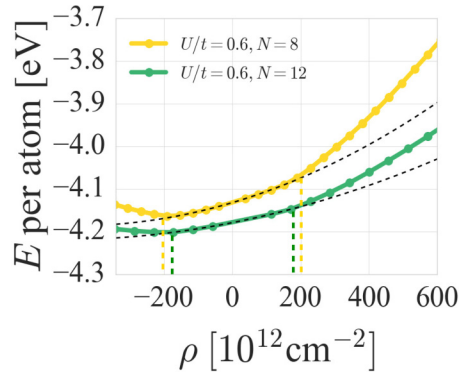

FIG. 3. The energy of the PHS broken phase for different amounts of doping ρ for $N = 8$ (yellow) and $N = 12$ (green) with $U/t = 0.6$ in the single-orbital model.

We examine the behavior of the energy of the nonmagnetic phase as the filling is shifted by an amount δn off half filling. Figure 3 shows the free energy as a function of doping for a $N = 8$ (yellow) and $N = 12$ (green) nanoribbon, with $U = 0.6$. Here, the doping is expressed in cm^{-2} units, $\rho = \delta n/S$ where $S = 8.38 \times 10^{-15}\ \mathrm{cm}^2$ is the area of the ribbon. For low δn, the free energy obtained numerically has a quadratic dependency on the doping,

$$F(U, n) = UN\left(1 + \frac{\rho S}{4N}\right)^2, \tag{6}$$

which corresponds to the interacting term of Eq. (4). It is worth noting that the Coulomb interaction breaks PHS, that is, the minimum of the total energy is no longer expected at half filling. For small hole doping values, the orbitals at the atomic edges become less populated at lower kinetic energy cost, as their coordination number is lower, whereas the Coulomb repulsion is lowered. For larger doping, $|\rho| > 200 \times 10^{12}\ \mathrm{cm}^{-2}$ or $\langle n \rangle \gtrsim 0.6$, a stronger dependency on ρ is observable, as the bulk bands become doped and the kinetic energy gain decreases. This occurs as the bulk occupation becomes comparable to the preferred occupation at the edge [see Fig. 1(d)], which is reduced as N increases (see below). Note that the kinks in the curve of Fig. 3 separates the small and large doping regimes, or equivalently, the edge and bulk doping regimes.

Figure 4(a) shows the Fermi energy as a function of U/t, where the two doping regimes are visible. The separation between the small and large doping regimes occurs around $|\rho| \approx 200 \times 10^{12}\ \mathrm{cm}^{-2}$. This is consistent with the peak of the density of states (DOS) around half filling (see Appendix).

For larger doping, however, the Fermi energy has a different functional (see Appendix). This dependency is still visible when U/t is varied between 0.2 and 1.6 for dopings up to $\rho = 10^{15}\ \mathrm{cm}^{-2}$, as shown in Fig. 4(b). We note that the conventional square root functional that corresponds to a linear dispersion can be recovered at this regime. While these results have been obtained in small systems, this behavior should scale to larger ribbons. The amount of doping at which the bulk states become filled in larger nanoribbons is reduced, as the band separation decreases with a power law [57] of $\sim 1/N$. This argument can also serve to interpret Fig. 3: The kink

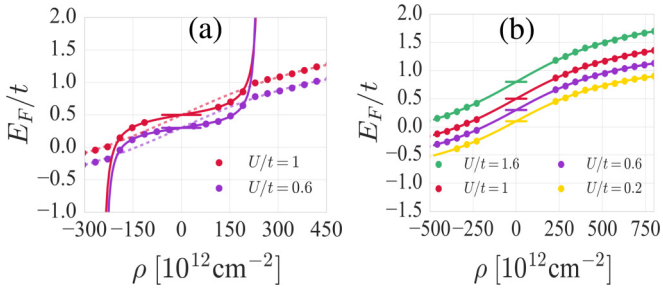

FIG. 4. The Fermi energy of the PHS broken solution for $N = 8$ and different U/t. The horizontal bar indicates the Fermi energy of the two magnetic phases at half filling. (a) For smaller doping the Fermi energy is fitted with a different functional (solid lines) as for the larger doping (dashed lines, see text). (b) Fermi energy within the large doping regime for four different Hubbard parameters: $U/t = 0.2$, 0.6, 1.0, and 1.6.

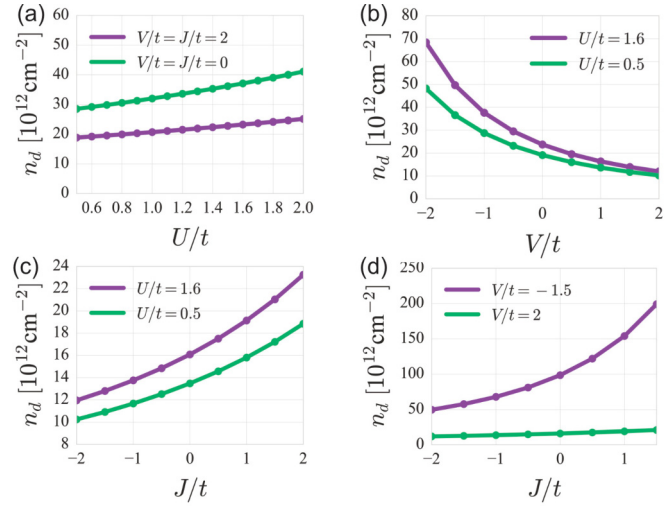

FIG. 5. Total d-state occupation of a ribbon with $N = 8$ plotted for different interacting parameters. Both FM and AFM phase have identical occupation.

separating small and large doping regime appears at lower ρ as N increases. This suggests that in larger graphene nanostructures, the doping required to reach the energetic minimum decreases, which may serve as an explanation to the elusive measurement of magnetic edges in graphene ribbons, which was previously unaccounted for. Note that the absent curves for $U/t = 1.6$ and 0.2 of Fig. 4(a) are numerically costly and adds little information, and hence, are omitted from this paper.

The implications of the mean-field level results obtained in this section can be summarized as follows: (i) A finite hole doping minimizes the energy functional, and hence, the half-filled state is no longer the most favored one and (ii) under realistic conditions, larger nanoribbons onto acceptor substrates would not necessarily show magnetism, but rather a hole, PHS broken state.

2. *Multi-orbital model*

We consider next the multi-orbital model by including the d_{xz} and d_{yz} orbitals, which breaks PHS even at a single-particle level. These bands are known to have a finite occupation and yield relevant effects [37]. Note that the magnetic solutions observed so far appear only at half filling, within the PHS condition, and thus, are not guaranteed in an implicitly broken PHS system. Moreover, including these orbitals allows us to elucidate the role of the interacting parameters V and J of Eq. (4) on the different solutions, which are absent in the single-orbital model. We define δn_p and δn_d as the p_z- and d-orbital doping, respectively, such that $\rho = \delta n_p + \delta n_d$. The half-filling condition reads $\delta n_p = -\delta n_d$, where the orbital occupation per spin is given by $n_p = 0.5 + \delta n_p$ and $n_d = \delta n_d$, respectively. This leads to a renormalization of the orbital energies, namely,

$$E_\alpha(\delta n_\alpha) = \sum_\sigma [E_d + \delta n_\alpha(2V - J)]\hat{n}_{\alpha\sigma}, \tag{7}$$

where we can infer that a decreased energetic separation of p_z and d orbitals lead to enhancement of the d-band occupation and vice versa.

Figure 5 shows n_d as a function of the interacting parameters in units of t. When V and J are kept constant, an increased U leads to a larger occupation of the d orbitals [see Fig. 5(a)], as the Coulomb repulsive interaction is larger at the occupied p_z orbitals. For negative V or positive J, the d-orbital occupation becomes larger, as the d-orbital energy shift is reduced, as is shown in (b) and (c), respectively. Finally, Fig. 5(d) shows that typical positive V values yield small d-band occupation for any J, whereas negative V results in d occupation up to two orders of magnitude larger. We stress, however, that the repulsive (physical) Coulomb interaction yields $V, J > 0$.

Figure 6 shows the local magnetization and orbital doping of a 48-sites ribbon in the AFM phase, with $U = 1.6t$ and $J = 0.5t$. An attractive d-orbital Coulomb interaction $V = -2t$ (red) results in an enhanced d-orbital magnetization at the sites next to the edge, whereas the single orbital results are recovered for a repulsive d-orbital Coulomb interaction $V = 2t$ (black). Finally, we consider the multi-orbital doped solution. Figure 7(a) shows the d-orbital doping as a function of total doping, $\rho = (\delta n_p + \delta n_d)/S$ for positive (green), zero (purple), and negative (yellow) p-d Coulomb interaction V. A quadratic law is observed for the latter, whereas a slow, linear

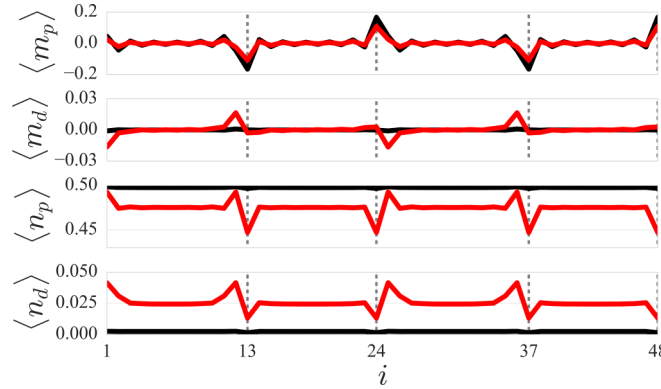

FIG. 6. The expectation value of the magnetization $m_{p/d}$ and occupation $n_{p/d}$ per site and spin for a ribbon with $N = 12$ in the AFM phase, where $U = 1.6t$ and $J = 0.5t$, with $V = -2t$ (red) and $V = 2t$ (black).

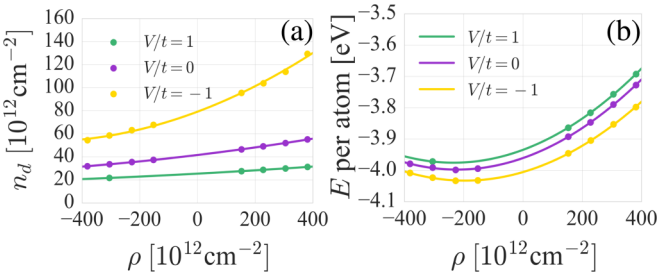

FIG. 7. Results for a nanoribbon with $N = 8$, for $U/t = 1$ and $J/t = 1$. (a) Total d-state occupation and (b) energy of the nonmagnetic phase for different doping strengths n for $V/t = 1, 0$, and -1.

increase in d-orbital occupation occurs for the former. The free-energy functional at low doping results now in

$$F(\rho, U, V, J) = UN\left(1 + \frac{\delta n_p}{4N}\right)^2 + (2V - J)n_p\delta n_d, \quad (8)$$

where $n_p = \rho S - \delta n_d$. The first term dominates, and was already observed in the single-orbital model [see Eq. (6)]. For larger dopings, the kinetic energy raises, and the single-orbital results are recovered, with the total minimum appearing for similar doping values. The inclusion of d orbitals does not lead to qualitative differences for the free energy or the character of the ground state, compared to the single-orbital model, unless for the negative V case. We stress that both AFM and FM solutions are encountered also when PHS is implicitly broken, which was not clear *a priori*.

IV. CONCLUSIONS

We have examined three different edge phases in terms of local magnetization and local orbital occupation, both in the single and in the multi-orbital model, of graphene nanoribbons with zigzag edges. For half filling and finite interaction strengths the interedge super exchange mechanism results in a lower free energy of the AFM phase compared to the FM phase, as expected. The PSH symmetry broken phase shows a minimum in the free energy at the boundary between the small and the large hole doping regime. In the former regime, the local doping occurs exclusively at the edge atoms, lowering the energy via exchange, whereas in the latter, the doping spreads throughout the bulk, lowering the kinetic energy and hence, increasing the free energy. These result are unchanged in a multi-orbital model, where a magnetic solution is also encountered in the broken PHS system. We observe, however, that the d bands acquire a prominent role for certain values of the Coulomb interaction, V and J. Thus, the multi-orbital computations confirm that the single-orbital description remains a good approximation for the energy gap of the two magnetic phases, whereas the d-band occupation is sensitive to the Coulomb interaction parameters. In the thermodynamic limit (large N, small interactions) the free energy of the three edge phases coincide, and hence, observation of a magnetic state would require very low temperatures, small ribbon sizes, and specific low-interacting, acceptor substrates.

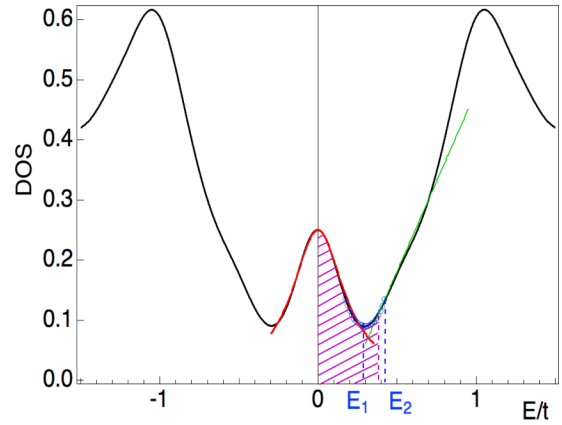

FIG. 8. DOS of a graphene nanoribbon (black curve). The zero of the energy is conveniently defined at half filling $\rho = 0$, where a peak due to the edge bands is apparent (see Fig. 1). A fit to this peak is encountered with the function $g(E) = g_0[1 + (\chi E)^2]^{-1}$ (red curve) for $|E| < E_1$. We find the fitting function $h(E) = h_0[\cos^2(\chi E)]^{-1}$ for $E_1 < |E| < E_2$ (blue dots), with $E_m \sim (E_2 - E_1)/2$. For larger energies, $E_2 < E < t$ the DOS is roughly linear (green line).

ACKNOWLEDGMENTS

This work is supported/funded by the Cluster of Excellence "CUI: Advanced Imaging of Matter" of the Deutsche Forschungsgemeinschaft (DFG) - EXC 2056 - Project ID 390715994. We thank A. Chudnovskiy and R. H. Blick for fruitful discussions.

APPENDIX: DENSITY FUNCTIONAL OF THE FERMI LEVEL

We define for convenience the zero energy at half filling $E_{\rm hf} = 0$. The DOS of the nanoribbon is plotted in Fig. 8 (black curve): A peak around $E_{\rm hf}$ is due to the edge bands [see Fig. 1(c)] and is fitted for $|E| < E_1$ with $g(E) = g_0[1 + (\chi E)^2]^{-1}$ (red curve), with g_0, χ being unimportant parameters for this discussion. For $E_1 < E < E_2$ the fitting function $h(E) = h_0 \cos^{-2}(\chi(E - E_m))$ can be encountered (blue dots), whereas for $E > E_2$, which is roughly the bandwidth of the edge bands, the DOS increases linearly with energy, $\mathrm{DOS}(E) \simeq E_0 + \beta E$ (green line), which is typical for the Dirac dispersion.

It follows that the Fermi energy can be obtained by direct integration. In the low doping regime, $|E_F| \lesssim E_1$ we have

$$\rho(E_F) = \int_0^\infty f(E)\mathrm{DOS}(E)dE \simeq \int_0^{E_F} \frac{a}{1 + (\chi E)^2} dE$$
$$= \frac{g_0}{\chi} \arctan\{\chi E_F\},$$

where we have employed the low temperature limit, $f(E) \simeq \Theta(E - E_F)$. We thus concur that a possible Fermi energy's density functional is a tangent,

$$E_F \propto \tan\left(\frac{\rho\chi}{g_0}\right).$$

For $E_1 < |E_F| < E_2$, as in Fig. 8, the doping corresponds to the shaded area below the curve, that is

$$\rho(E_F) \simeq \frac{g_0}{\chi}\arctan(\chi E_1) + \int_{E_1}^{E_F} \frac{h_0}{\cos^2(\chi E)} = \frac{g_0}{\chi}\arctan(\chi E_1) + \frac{h_0}{\chi}(\tan\chi E_F - \tan\chi E_1),$$

giving now a different functional

$$E_F \propto \arctan\left(\frac{\rho\chi}{h_0}\right).$$

The boundary between both regimes corresponds to $E_1 \simeq 0.3t$, which explains the switching behavior of Fig. 4(a). For Fermi energies larger than E_2 we would recover the linear dispersion, yielding the usual squareroot density functional for the Fermi energy, which behaves similarly as the arctan one within the doping values considered in this paper. We stress that the functionals obtained above are arbitrary, as similar ones can be derived. The important fact and the aim of this Appendix is to illustrate the change of behavior due to the finite size effects, which manifest here as edge population.

[1] M. Fruchart and D. Carpentier, C. R. Phys. **14**, 779 (2013).
[2] J. K. Asbóth, L. Oroszlány, and A. Pályi, *A Short Course on Topological Insulators, Band Structure and Edge States in One and Two Dimensions*, Lecture Notes in Physics, Vol. 919 (Springer, Cham, 2016).
[3] D. Gosálbez-Martínez, D. Soriano, J. Palacios, and J. Fernández-Rossier, Solid State Commun. **152**, 1469 (2012).
[4] O. V. Yazyev, R. B. Capaz, and S. G. Louie, Phys. Rev. B **84**, 115406 (2011).
[5] O. V. Yazyev, Rep. Prog. Phys. **73**, 056501 (2010).
[6] O. V. Yazyev and M. I. Katsnelson, Phys. Rev. Lett. **100**, 047209 (2008).
[7] M. Wimmer, I. D. I. M. C. Adagideli, S. M. C. Berber, D. Tománek, and K. Richter, Phys. Rev. Lett. **100**, 177207 (2008).
[8] F. Muñoz-Rojas, J. Fernández-Rossier, and J. J. Palacios, Phys. Rev. Lett. **102**, 136810 (2009).
[9] N. Friedrich, P. Brandimarte, J. Li, S. Saito, S. Yamaguchi, I. Pozo, D. Peña, T. Frederiksen, A. Garcia-Lekue, D. Sánchez-Portal, and J. I. Pascual, Phys. Rev. Lett. **125**, 146801 (2020).
[10] J. Li, S. Sanz, N. Merino-Díez, M. Vilas-Varela, A. Garcia-Lekue, M. Corso, D. G. de Oteyza, T. Frederiksen, D. Peña, and J. I. Pascual, Nat. Commun. **12**, 5538 (2021).
[11] Y. Kobayashi, K.-i. Fukui, T. Enoki, K. Kusakabe, and Y. Kaburagi, Phys. Rev. B **71**, 193406 (2005).
[12] Y. Shibayama, H. Sato, T. Enoki, and M. Endo, Phys. Rev. Lett. **84**, 1744 (2000).
[13] V. L. J. Joly, M. Kiguchi, S.-J. Hao, K. Takai, T. Enoki, R. Sumii, K. Amemiya, H. Muramatsu, T. Hayashi, Y. A. Kim, M. Endo, J. Campos-Delgado, F. López-Urías, A. Botello-Méndez, H. Terrones, M. Terrones, and M. S. Dresselhaus, Phys. Rev. B **81**, 245428 (2010).
[14] Y. Y. Li, M. X. Chen, M. Weinert, and L. Li, Nat. Commun. **5**, 4311 (2014).
[15] C. Tao, L. Jiao, O. V. Yazyev, Y.-C. Chen, J. Feng, X. Zhang, R. B. Capaz, J. M. Tour, A. Zettl, S. G. Louie, H. Dai, and M. F. Crommie, Nat. Phys. **7**, 616 (2011).
[16] G. Z. Magda, X. Jin, I. Hagymási, P. Vancsó, Z. Osváth, P. Nemes-Incze, C. Hwang, L. P. Biró, and L. Tapasztó, Nature (London) **514**, 608 (2014).
[17] C. L. Kane and E. J. Mele, Phys. Rev. Lett. **95**, 226801 (2005).
[18] C. L. Kane and E. J. Mele, Phys. Rev. Lett. **95**, 146802 (2005).
[19] N. Goldman, W. Beugeling, and C. M. Smith, Europhys. Lett. **97**, 23003 (2012).
[20] S. Rachel, Rep. Prog. Phys. **81**, 116501 (2018).
[21] D. Zheng, G.-M. Zhang, and C. Wu, Phys. Rev. B **84**, 205121 (2011).
[22] M. Hohenadler, F. Parisen Toldin, I. F. Herbut, and F. F. Assaad, Phys. Rev. B **90**, 085146 (2014).
[23] J. Cao and S.-J. Xiong, Phys. Rev. B **88**, 085409 (2013).
[24] M. Luo, Phys. Rev. B **102**, 075421 (2020).
[25] D. Soriano and J. Fernández-Rossier, Phys. Rev. B **82**, 161302(R) (2010).
[26] J. Lado, N. García-Martínez, and J. Fernández-Rossier, Synth. Met. **210**, 56 (2015).
[27] J. Jung, T. Pereg-Barnea, and A. H. MacDonald, Phys. Rev. Lett. **102**, 227205 (2009).
[28] J. Fernández-Rossier, Phys. Rev. B **77**, 075430 (2008).
[29] K. Wakabayashi, M. Sigrist, and M. Fujita, J. Phys. Soc. Jpn. **67**, 2089 (1998).
[30] J. Jung and A. H. MacDonald, Phys. Rev. B **79**, 235433 (2009).
[31] X. F. Fan, W. T. Zheng, V. Chihaia, Z. X. Shen, and J.-L. Kuo, J. Phys.: Condens. Matter **24**, 305004 (2012).
[32] F. Varchon, R. Feng, J. Hass, X. Li, B. N. Nguyen, C. Naud, P. Mallet, J.-Y. Veuillen, C. Berger, E. H. Conrad, and L. Magaud, Phys. Rev. Lett. **99**, 126805 (2007).
[33] H. Henck, D. Pierucci, G. Fugallo, J. Avila, G. Cassabois, Y. J. Dappe, M. G. Silly, C. Chen, B. Gil, M. Gatti, F. Sottile, F. Sirotti, M. C. Asensio, and A. Ouerghi, Phys. Rev. B **95**, 085410 (2017).
[34] J. H. Correa, A. Pezo, and M. S. Figueira, Phys. Rev. B **98**, 045419 (2018).
[35] M. Polini, A. Tomadin, R. Asgari, and A. H. MacDonald, Phys. Rev. B **78**, 115426 (2008).
[36] H. Feldner, Z. Y. Meng, A. Honecker, D. Cabra, S. Wessel, and F. F. Assaad, Phys. Rev. B **81**, 115416 (2010).
[37] S. Konschuh, M. Gmitra, and J. Fabian, Phys. Rev. B **82**, 245412 (2010).
[38] J. Sichau, M. Prada, T. Anlauf, T. J. Lyon, B. Bosnjak, L. Tiemann, and R. H. Blick, Phys. Rev. Lett. **122**, 046403 (2019).
[39] M. Prada, Phys. Rev. B **103**, 115425 (2021).
[40] M. Prada, L. Tiemann, J. Sichau, and R. H. Blick, Phys. Rev. B **104**, 075401 (2021).
[41] J. C. Slater and G. F. Koster, Phys. Rev. **94**, 1498 (1954).
[42] D. Gosálbez-Martínez, J. J. Palacios, and J. Fernández-Rossier, Phys. Rev. B **83**, 115436 (2011).
[43] L. Pisani, J. A. Chan, B. Montanari, and N. M. Harrison, Phys. Rev. B **75**, 064418 (2007).

[44] S.-i. Kuroda and H. Shirakawa, Phys. Rev. B **35**, 9380 (1987).
[45] J. Hubbard, Proc. R. Soc. London A **276**, 238 (1963); **277**, 237 (1964); **281**, 401 (1964).
[46] P. Fazekas, *Lecture Notes on Electron Correlation and Magnetism*, Series in Modern Condensed Matter Physics, Vol. 5 (World Scientific, Singapore, 1999).
[47] H. Hadipour, E. Şaşıoğlu, F. Bagherpour, C. Friedrich, S. Blügel, and I. Mertig, Phys. Rev. B **98**, 205123 (2018).
[48] Y. Claveau, B. Arnaud, and S. D. Matteo, Eur. J. Phys. **35**, 035023 (2014).
[49] J. L. Lado and J. Fernández-Rossier, Phys. Rev. Lett. **113**, 027203 (2014).
[50] J. L. Lado and J. Fernández-Rossier, Phys. Rev. B **90**, 165429 (2014).
[51] X. Wan, A. M. Turner, A. Vishwanath, and S. Y. Savrasov, Phys. Rev. B **83**, 205101 (2011).
[52] Y.-W. Son, M. L. Cohen, and S. G. Louie, Phys. Rev. Lett. **97**, 216803 (2006).
[53] S. Ganguly, M. Kabir, and T. Saha-Dasgupta, Phys. Rev. B **95**, 174419 (2017).
[54] J. Kunstmann, C. Özdoğğan, A. Quandt, and H. Fehske, Phys. Rev. B **83**, 045414 (2011).
[55] L. Veyrat, C. Déprez, A. Coissard, X. Li, F. Gay, K. Watanabe, T. Taniguchi, Z. Han, B. A. Piot, H. Sellier, and B. Sacépé, Science **367**, 781 (2020).
[56] E. H. Lieb, Phys. Rev. Lett. **62**, 1201 (1989).
[57] K. Wakabayashi, K.-I. Sasaki, T. Nakanishi, and T. Enoki, Sci. Techn. Adv. Mater. **11**, 054504 (2010).